IEEE Robotics and Automation Letters (RA-L) paper, presented at ICRA 2026, Vienna, Austria. Cite as RA-L paper.

Design, Modeling, and Experimental Characterization of a Rod-Driven Continuum Robot With Asymmetric Joints for Active Chest Catheters

Mohammadmehdi Lari and Matteo Russo

***Abstract*—Thoracostomy involves draining fluid from the pleural cavity using chest tubes. This medical intervention is currently performed manually by inserting a hollow flexible tube, risking damage to vital organs, including the lungs, diaphragm, spleen, and mediastinum, due to the lack of control over the tube's path inside the patient's body. Inspired by snake-like structures, continuum robots are particularly well-suited to address the challenges encountered during thoracostomy. Taking advantage of their slender shape, they can nest inside the tubes and guide them from within without requiring further incision. However, available continuum robots are not suitable for this application due to geometrical and payload requirements. In this letter, a novel design is presented, leveraging a multi-backbone structure with asymmetrical rolling joints to enhance payload capacity and dexterity while maintaining the slender shape of the robot. A static modeling approach is proposed to estimate the configuration of the robot given the force applied to the robot, including the effects of friction and gravity often neglected for these robots. Two prototypes were 3D-printed, allowing for after-use disposal due to their cost-effectiveness, thereby preventing cross-contamination. Stiffness and position error were evaluated for the prototypes, demonstrating a modeling accuracy of 2.25%.**

***Index Terms*—Continuum robots, kinematics, mechanism design, soft robot materials and design, tendon/wire mechanism.**

I. Introduction

THORACOSTOMY is a high-risk medical procedure that involves draining a fluid from the pleural cavity via chest tubes, with complication rates reported as high as 40%. Many of these complications arise from improper tube positioning or inadvertent damage to internal organs during insertion, which is typically performed blindly [1] and with no control over the tube's path (Fig. 1).

Continuum robots, due to their slender shape, can fit inside these chest tubes and guide them from inside. They can reduce the complication rates of this medical operation by providing control over the tube's path to avoid damaging internal organs and facilitate proper tube positioning. Furthermore, sensing the robot's configuration gives feedback on the tube's shape to increase procedural safety.

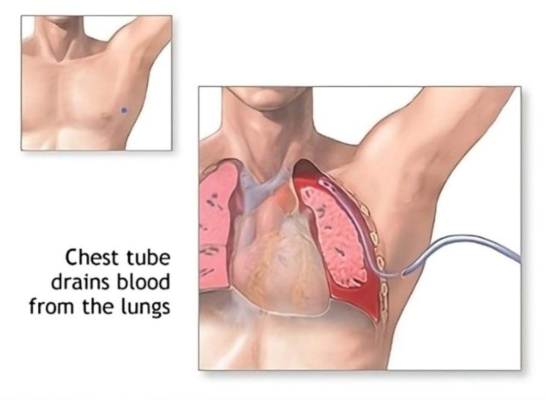

Fig. 1. Schematic of chest tube insertion [4].

However, this task presents significant medical and technical challenges. First of all, the medical environment requires the robot to be either sterilizable at a high temperature or disposable after usage (and thus inexpensive) to prevent cross-contamination. Moreover, the entire robot's length has to be steerable to enable proper tube positioning. The force capacity of continuum robots is generally low, limited by their structural properties such as stiffness and range of motion [2]. Since the tubes have a high slenderness ratio, it becomes difficult to manipulate them due to the reduced force capacity. Further, compliance is crucial for safety in medical continuum robots. An increase in stiffness would result in reduced compliance [3], impeding the expansion of the lungs.

To address these challenges, a novel rod-driven, multi-backbone design with asymmetric rigid links and rolling joints is proposed. This asymmetric design increases the leverage of the active rod without extending the diameter of the robot, which allows for a higher force capacity while maintaining compliance. Additionally, a static modeling approach was developed to predict the robot's configuration from the applied tension force. To validate the robot's effectiveness in manipulating the chest tube and ensure the accuracy of the proposed modeling approach, a prototype was 3D-printed and experimentally characterized; this manufacturing solution also facilitates disposability due to its cost-effectiveness.

Received 25 March 2025; accepted 23 July 2025. Date of publication 11 August 2025; date of current version 19 August 2025. This article was recommended for publication by Associate Editor A. Han and Editor Y. Park upon evaluation of the reviewers' comments. *(Corresponding author: Matteo Russo.)*

The authors are with the Department of Industrial Engineering, School of Engineering, University of Rome Tor Vergata, 00133 Rome, Italy (e-mail: matteo.russo@uniroma2.it).

This article has supplementary downloadable material available at https://doi.org/10.1109/LRA.2025.3597860, provided by the authors.

Digital Object Identifier 10.1109/LRA.2025.3597860

The contribution of this work can be summarized in the following points:

- Chest tubes are currently inserted manually, using a rigid straight core to provide stiffness during part of the insertion, which is then gradually pulled out of the tube. This makes reaching the target pose, with the tip of the tube close to the desired aspiration point, difficult, critically reducing the effectiveness of the tube. The proposed design provides a way to guide the tube up to the desired point, thanks to its active degrees of freedom, while maintaining the disposability of the system, thanks to its limited cost.
- The proposed architecture employs asymmetric rigid links with rolling joints, previously seen mostly in lower-mobility hands, for a novel hyper-redundant architecture that achieves a higher payload while maintaining a slender form factor (6.2 mm outer diameter, backbone length of 375.0 mm, for a 60.5 length-to-diameter ratio).
- A static modeling approach is proposed to predict the robot configuration and enable shape sensing from motor torque measurements. This model realizes an efficient compromise between accuracy and computational cost by including static and friction parameters and modeling the actuating NiTi rods through the Capstan equation. Experiments performed on a 3D-printed prototype demonstrated its effectiveness in manipulating the tube and the accuracy of the proposed model, with 2.25% error with respect to robot length (PCC model: 11.45% error) while maintaining much better computation times (approx. 44 Hz) than differential (e.g., Cosserat) models.

II. Requirements

In this section, we will analyze the challenges presented by the task, which result in specific requirements for the robot's design. Some of these requirements arise due to compatibility with the medical setting, while others stem from technical constraints such as the robot's size, kinematic and kinetic properties, and actuation mechanism.

A. Medical Requirements

In a clinical environment, equipment must be purged of all living organisms through sterilization, thereby preventing the transmission of infection between patients. Medical devices are classified into three categories based on the level of sterility required: critical, semi-critical, and non-critical [5]. Since chest tubes directly come in contact with bodily fluids and open tissues, their sterilization is deemed critical.

Hospitals predominantly use thermal sterilization techniques due to their low cost and safety hazards. In order to destroy cells and microorganisms, the materials must withstand high temperatures, often accompanied by steam. Radiation-based and chemical methods offer a wider range of material compatibility; however, the former is rarely used in hospitals due to its safety hazards, whereas the latter has limitations when dealing with crevices and internal channels [6].

Therefore, ensuring sterilizability would necessitate high-quality metals, which must be machined at high costs due to their small dimensions. Alternatively, additive manufacturing allows for cost-effective fabrication, facilitating disposability.

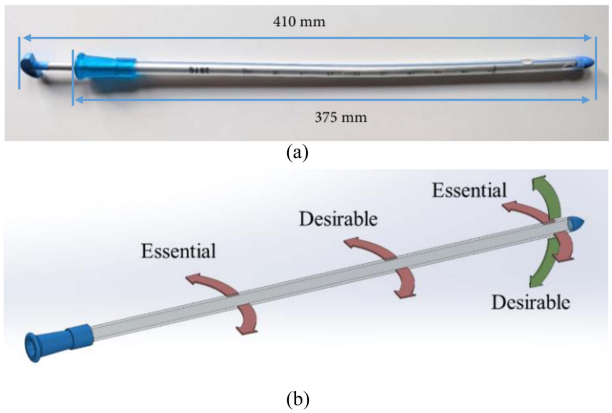

Fig. 2. 28F chest tube: (a) Commercial model with rigid inner core; (b) required degrees of freedom for active insertion.

B. Technical Requirements

Chest tubes come in different shapes and sizes, often expressed in French units, equal to one-third of a centimeter. The proper sizing is determined by the flow rate that the tube can accommodate, the properties of the fluid being evacuated, and its rate of formation [7]. Large-bore tubes are associated with a higher complication rate [1]. For this reason, a common large bore tube with an outer diameter of 28F was chosen for this task. The robot's dimensions are determined by the tube size shown in Fig. 2(a), resulting in an internal 6.2 mm diameter and a length of 375.0 mm.

Tube insertion is the most critical part of the operation. The robot must bend inside the chest wall before it reaches the visceral pleura to avoid damaging the internal organs. The thickness of the chest wall ranges from 26.6 to 80.2 mm, with an average of 48.6 mm as reported in [8] and [9]. Consequently, achieving a radius of curvature smaller than 20 mm ensures that the robot can bend within the chest wall.

At least two degrees of freedom (DoF) are required for the task (Fig. 2(b)). The tube tip interacts with anatomical tissue and sets the path for the rest of the tube; therefore, one DoF at the tip is essential for navigation. Another one is required at the base to maintain a sharp bending angle at the insertion point throughout the operation. Adding another DoF in the middle can enhance the robot's dexterity, and an extra DoF at the tip allows for navigation inside the sagittal plane. A list of the requirements is laid out in Table I.

III. Design and Modeling

The first step in the design process is to select an architecture and actuation mechanism. Continuum robots are categorized into intrinsically and extrinsically actuated robots, depending on where the actuation takes place. Intrinsic actuators are located directly on the robot itself and form a part of its backbone [10]. In contrast, extrinsic actuators are separated from the backbone and only act on it through force-transmitting mechanisms. The

TABLE I
REQUIREMENTS

Requirement	Numerical Value	Essential (E)/ Desirable (D)
Length	375.0 mm	E
Outer diameter	6.2 mm	E
Inner diameter	3.0 mm	D
Degrees of freedom	2 (Base, Tip)	E
	4 (Base, Tip x2, Mid)	D
Bending range (Base)	90 deg	E
	180 deg	D
Bending range (Tip X)	90 deg	E
Bending range (Mid)	90 deg	D
Bending range (Tip Y)	90 deg	D
Max radius of curvature	20.0 mm	E
Estimated Tension	10 – 100 N	E
Payload at the tip	> 0.35 N	E
Compliance under load	-	E
Sterilizable/Disposable	-	E

remote actuation eliminates the robot's size dependency on the actuators and allows for a much leaner design [11]. Besides, it facilitates robot sterilization or disposability by removing the onboard electronics, while the actuators can be hermetically sealed to prevent contamination.

Tendon-driven and concentric tube architectures are the most common among continuum robots. While concentric tube robots are often slenderer, they exhibit lower force capacity, limited workspace [12], and snapping behavior [2]. Therefore, an extrinsically actuated tendon-driven architecture is best suited for our application. Among these robots, the structures utilizing discrete rigid links with rolling joints, such as those in [13] and [14], achieve the highest force capacity relative to their slenderness ratio. Building on this concept, this section proposes a design based on the aforementioned architecture.

A. Mechanical Design

A prototype was designed containing three sections, each providing one degree of freedom (Fig. 3(a)). The sections are composed of rolling joints with connector links in between that facilitate tendon routing (Fig. 3(b)).

This robot has negligible inherent stiffness as the tube acts as an external backbone. The rolling joints have a circular profile, which is symmetrical for the distal sections' joints (Sections 2–3), similar to other continuum robots with this design [14]. Since the proximal section only needs to navigate away from the internal organs, different asymmetrical one-sided rolling joints are instead proposed for this section to increase the leverage of the actuating tendon and the section's range of motion in the direction of interest, consequently enhancing the force capacity (Fig. 3(c)). This asymmetric design (Fig. 4(a)) is obtained with a flat top for higher fabrication quality during additive manufacturing by alleviating the need for support. The profile of the rolling joint consists of two tangent arcs with different radii R_1 and R_2. The centerline of the two arcs is not placed in the middle of the link, but at distances A_1 and A_2 from the tendon holes, which increases the leverage of the farther tendon, resulting in higher torque and payload capacity. As shown in Table II, by changing the lever arm of the tendons from 2 mm in the symmetric design

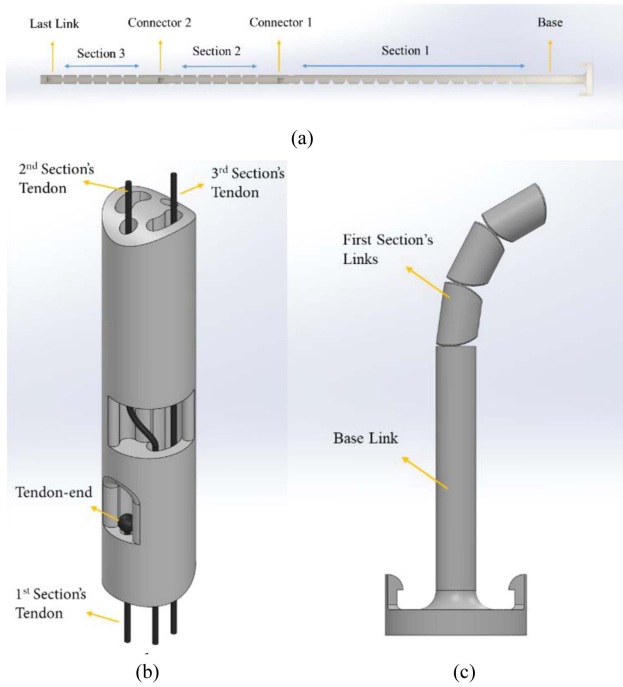

Fig. 3. Prototype design: (a) Link arrangement in the designed prototype; (b) connector link design for tendon routing and fixation; (c) First section with asymmetrical links and base link equipped with grippers to attach to the tube.

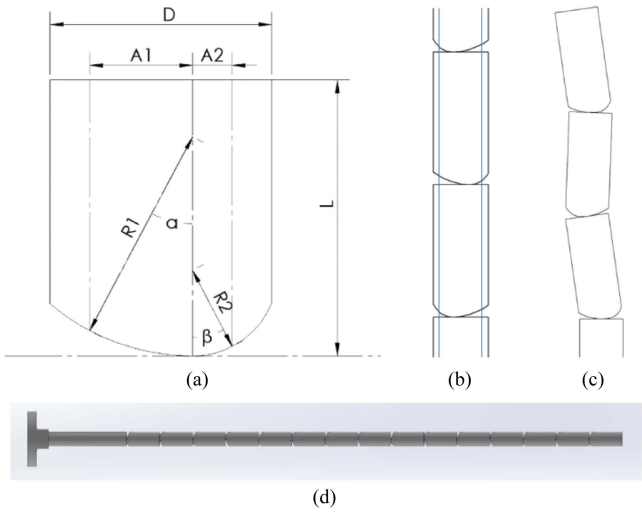

Fig. 4. Asymmetric joint design: (a) Side view of an individual link with geometrical parameters; (b) link sequence; (c) section buckling; (d) side view of the upgraded design.

TABLE II
DESIGN PARAMETERS

Parameter	Value	Description
L	15 mm	Link length
D	6.2 mm	Link diameter
n	15	The number of joints in the section
R_1	6.7 mm	Radius of the larger arc in the joint profile
R_2	2.275 mm	Radius of the smaller arc in the joint profile
A_1	3 ± 0.5 mm	Larger distance between the rods and the line of centers of the arcs
A_2	1 ± 0.5 mm	Smaller distance between the rods and the line of centers of the arcs

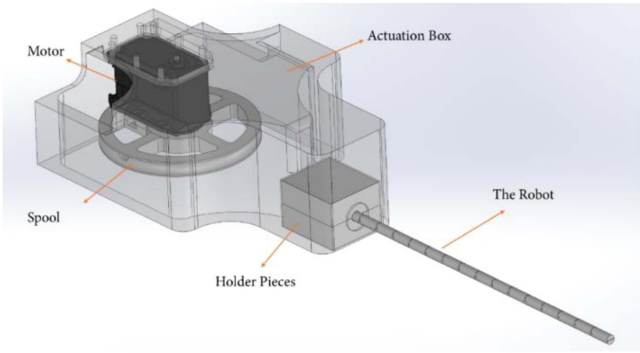

Fig. 5. Actuation system and the robot.

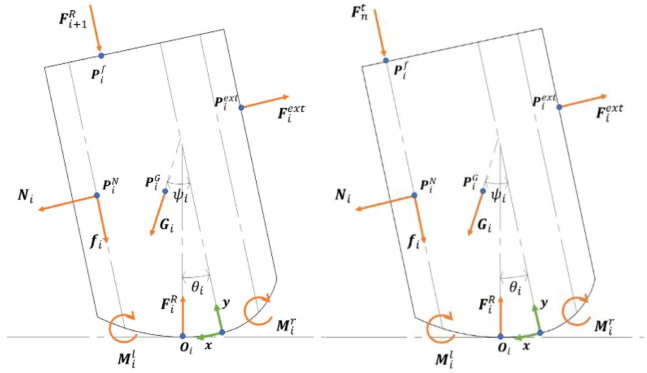

(a) (b)

Fig. 6. Free body diagrams: (a) Odd-numbered links, except for the distal one; (b) the distal link.

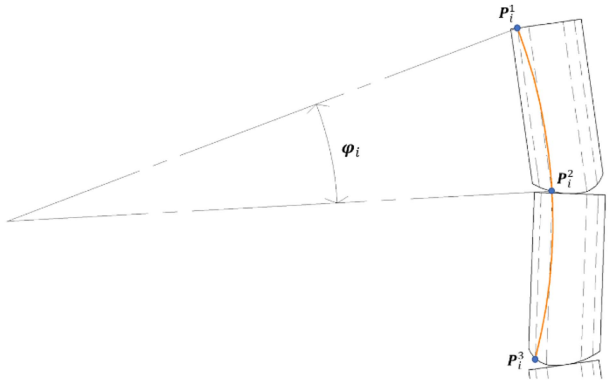

Fig. 7. Definition of parameter φ_i.

to 3 mm (A1) and 1 mm (A2), this design respectively doubles and halves the mechanical advantage when bending the section in those directions if we assume the same tendon tension.

To enable motion in both directions, the joints can alternate sides while maintaining this increased leverage (Fig. 4(b)), though this compromises structural stability and can lead to buckling (Fig. 4(c)). To address this issue, a multi-backbone architecture was implemented by substituting the original braided fiber tendons with Nitinol rods, which introduce inherent stiffness into the system to minimize buckling and enhance force capacity. The length of each joint has been selected to allow bending radius up to the desired range of motion while minimizing the number of joints (thus minimizing buckling, enhancing stiffness, and simplifying manufacturing and assembly). However, this value can be easily modified without significantly affecting robot behavior.

Holder pieces were designed to grasp the base link and fix it in an actuation box, which contains all the actuation elements, including a Dynamixel MX-64T DC motor and a spool (Fig. 5). The Nitinol rods are attached to the spool and pulled by the motor to bend the robot.

B. Modeling

This section presents a static modeling approach for the latest design, focusing on the novel asymmetric design. Static equilibrium equations are written for each link to achieve a set of simultaneous equations that can be solved numerically to obtain the joints' bending angle under the specified tension force. A few assumptions are made to keep the model from being overly complex, including:

- The Nitinol rods remain linearly elastic within the robot's range of motion.
- The motion is confined within a plane.
- The friction between the rods and the links can be modeled with the Capstan friction theorem.
- The equivalent normal contact force acts on the middle point of the active tendon hole.
- Link deformations and joint slips can be ignored.

The forces exerted on the odd-numbered links are shown in Fig. 6. They include the tension force applied by the fixed rod ($\boldsymbol{F}_n^t$) at $\boldsymbol{P}_i^f$, the reaction forces applied by the upper link ($\boldsymbol{F}_{i+1}^R$) and to the link below ($\boldsymbol{F}_i^R$), normal contact force ($\boldsymbol{N}_i$) and friction force ($\boldsymbol{f}_i$) that the rod exerts on the link at $\boldsymbol{P}_i^N$, gravity ($\boldsymbol{G}_i$) applied at the center of mass ($\boldsymbol{P}_i^G$), external forces ($\boldsymbol{F}_i^{ext}$) applied at $\boldsymbol{P}_i^{ext}$, and the elastic resistivity of the left ($\boldsymbol{M}_i^l$) and right ($\boldsymbol{M}_i^r$) rods. The frame origin is located on the joint profile where the two arcs meet, with the y-axis pointing toward their centers and the x-axis pointing in the bending direction.

The tension force in each link (F_i^t) is approximated from the tension force in the link below (F_{i-1}^t) using the Capstan equation to consider the friction force with the coefficient of μ (1). This method is explained and proven effective in previous works such as [15].

$$\left|\boldsymbol{F}_i^t\right| = F_{i-1}^t \, e^{-\mu\varphi_i} \tag{1}$$

The definition of φ_i in (1) is illustrated in Fig. 7. This angle would be equivalent to the bending angle of the section in an ideal case, but it differs in the real case because of the clearance between the tendon routing path diameter and the diameter of the tendon/rod cross-section. As such, the theoretical centerline of the tendon and the centerline of its desired paths differ, creating localized contacts that generate friction at specific points. $\boldsymbol{P}_i^1$ and $\boldsymbol{P}_i^2$ are located on the sides of the active tendon hole and form a circle with $\boldsymbol{P}_i^3$. The angle between $\boldsymbol{P}_i^1$ and $\boldsymbol{P}_i^2$ on this circle is considered equivalent to the angle swept by the tendon on a pulley in Capstan equation.

$$\boldsymbol{P}_i^1 = \begin{bmatrix} A_i^l + c \\ L \end{bmatrix} \tag{2}$$

IEEE Robotics and Automation Letters (RA-L) paper, presented at ICRA 2026, Vienna, Austria. Cite as RA-L paper.

$$\boldsymbol{P}_i^2 = \begin{bmatrix} A_i^l - c \\ R_i^l\left(1-\cos\alpha_i\right) \end{bmatrix} \tag{3}$$

$$\boldsymbol{P}_i^3 = \begin{bmatrix} \left(A_i^l - R_i\theta_i + c\right)\cos\theta_i + R_i\sin\theta_i + L\sin\theta_i \\ \left(A_i^l - R_i\theta_i + c\right)\sin\theta_i + R_i\left(1-\cos\theta_i\right) - L\cos\theta_i \end{bmatrix} \tag{4}$$

Therefore, the tension force in each link can be calculated as a function of the applied tension force by the actuator F_0^t.

$$\left|\boldsymbol{F}_i^t\right| = F_0^t\, e^{-\mu \sum_{j=1}^{i} \varphi_j} \tag{5}$$

The friction force is the difference between F_i^t and F_{i-1}^t.

$$\left|\boldsymbol{f}_i\right| = F_0^t\, e^{-\mu \sum_{j=1}^{i-1} \varphi_j}\left(1 - e^{-\mu\varphi_i}\right) \tag{6}$$

Also, the normal contact force can be calculated by dividing the friction force by its coefficient.

$$\left|\boldsymbol{N_i}\right| = {}^{1}\!/_{\mu}\ \left|\boldsymbol{f}_i\right| \tag{7}$$

The elastic resistive moment applied by the Nitinol rods is given by (8) as discussed in [15], where E is the equivalent modulus of elasticity and I is the moment of inertia of the rod. The length of the rod that is not covered by the links is denoted by s, which is a function of the bending angle θ.

$$\left|\boldsymbol{M_i}\right| = {EI\theta_i}/{s_i\left(\theta_i\right)} \tag{8}$$

The gravitational force is directed at an angle of ψ_i, which indicates the orientation of the link in the space. It can be calculated from the initial configuration of the robot and the cumulative deformation up to that joint.

Now we can write the moment balance at $\boldsymbol{O}_i$ as

$$\begin{aligned} \sum \boldsymbol{M}_{\boldsymbol{O_i}} = 0 \Rightarrow\ & \boldsymbol{F}_{i+1}^R \times \left(\boldsymbol{P}_i^F - \boldsymbol{O}_i\right) + \left(\boldsymbol{N}_i + \boldsymbol{f}_i\right) \\ & \times \left(\boldsymbol{P}_i^N - \boldsymbol{O}_i\right) + \boldsymbol{G}_i \times \left(\boldsymbol{P}_i^G - \boldsymbol{O}_i\right) + \boldsymbol{F}_i^{ext} \\ & \times \left(\boldsymbol{P}_i^{ext} - \boldsymbol{O}_i\right) - \ \boldsymbol{M}_i^{elastic} = 0 \end{aligned} \tag{9}$$

The y-axis force balance equation for the last link becomes

$$\sum F_y = \ 0 \Rightarrow F_n^R\cos\theta_n - F_n^t - f_n - G_n\ \cos\psi_n = \ 0 \tag{10}$$

and for the rest of the links, we get

$$\sum F_y = \ 0 \Rightarrow F_i^R\cos\theta_i - F_{i+1}^R - f_i - G_i\ \cos\psi_i = \ 0 \tag{11}$$

The left- and right-hand side parameters of each link are indicated by a superscript of l and r, i.e., A_i^l, A_i^r, R_i^l, R_i^r correspond to A_1, A_2, R_1, R_2 for the odd-numbered links and to A_2, A_1, R_2, R_1 for the even-numbered links respectively. R_i is defined as the arc radius of the active joint profile. Since only left-side bending is considered in this work, it is given as

$$R_i = \begin{cases} R_i^l & \theta_i > 0 \\ R_i^r & \theta_i < 0 \end{cases} \tag{12}$$

The angles α_i and β_i are defined as

$$\alpha_i = \sin^{-1}{R_i^l}/{A_i^l} \tag{13}$$

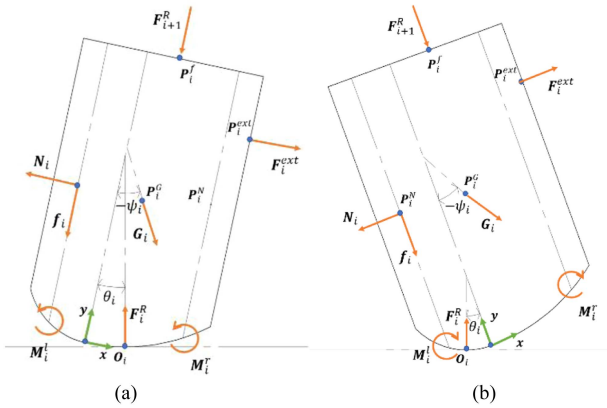

Fig. 8. Free body diagram of even-numbered links: (a) During buckling; (b) during normal motion.

$$\beta_i = \sin^{-1}{R_i^r}/{A_i^r} \tag{14}$$

Consequently, $s_i(\theta_i)$ for the left- and right-side rods will be

$$s_i^l\ \left(\theta_i\right) = \frac{R_i^l\left(1-\cos\left(\alpha_i - \theta_i\right)\right)}{\sin\theta}\,\theta_i \tag{15}$$

$$s_i^l\ \left(\theta_i\right) = \frac{R_i^r\left(1-\cos\left(\beta_i + \theta_i\right)\right)}{\sin\theta}\,\theta_i \tag{16}$$

The vectors connecting the origin to $\boldsymbol{O}_i$, $\boldsymbol{P}_i^N$, $\boldsymbol{P}_i^G$, and $\boldsymbol{P}_i^F$ are given by (17) through (20) for all of the odd-numbered links except for the last one (Fig. 8(a)).

$$\boldsymbol{O}_i = \begin{bmatrix} R_i\sin\theta_i \\ R_i\left(1-\cos\theta_i\right) \end{bmatrix} \tag{17}$$

$$\boldsymbol{P}_i^N = \begin{bmatrix} A_i^l \\ L_i^{tl}/2 + R_i^l\left(1-\cos\alpha_i\right) \end{bmatrix} \tag{18}$$

$$\boldsymbol{P}_i^G = \begin{bmatrix} \left(A_i^l + A_i^r\right)/2 - A_i^r - x_{CG} \\ L - y_{CG} \end{bmatrix} \tag{19}$$

$$\boldsymbol{P}_i^F = \begin{bmatrix} A_i^l - A_{i+1}^l + R_{i+1}\theta_{i+1} \\ L \end{bmatrix} \tag{20}$$

While (17)–(19) remain the same for the last link, $\boldsymbol{P}_n^F$ becomes

$$\boldsymbol{P}_n^F = \begin{bmatrix} A_i^l \\ L \end{bmatrix} \tag{21}$$

In the case of the even-numbered links, the x-axis is defined as positive in the right direction to simplify the equations, while θ_i is defined as positive when the link is bending on the left side, and $\boldsymbol{O}_i$ is given by (17) as before. However, $\boldsymbol{P}_i^N$, $\boldsymbol{P}_i^G$, and $\boldsymbol{P}_i^F$ become

$$\boldsymbol{P}_i^N = \begin{bmatrix} -A_i^l \\ L_i^{tl}/2 + R_i^l\left(1-\cos\alpha_i\right) \end{bmatrix} \tag{22}$$

$$\boldsymbol{P}_i^G = \begin{bmatrix} A_i^r - \frac{A_i^l + A_i^r}{2} - x_{CG} \\ L - y_{CG} \end{bmatrix} \tag{23}$$

$$\boldsymbol{P}_i^F = \begin{bmatrix} A_i^r - A_{i+1}^r - R_{i+1}\theta_{i+1} \\ L \end{bmatrix} \tag{24}$$

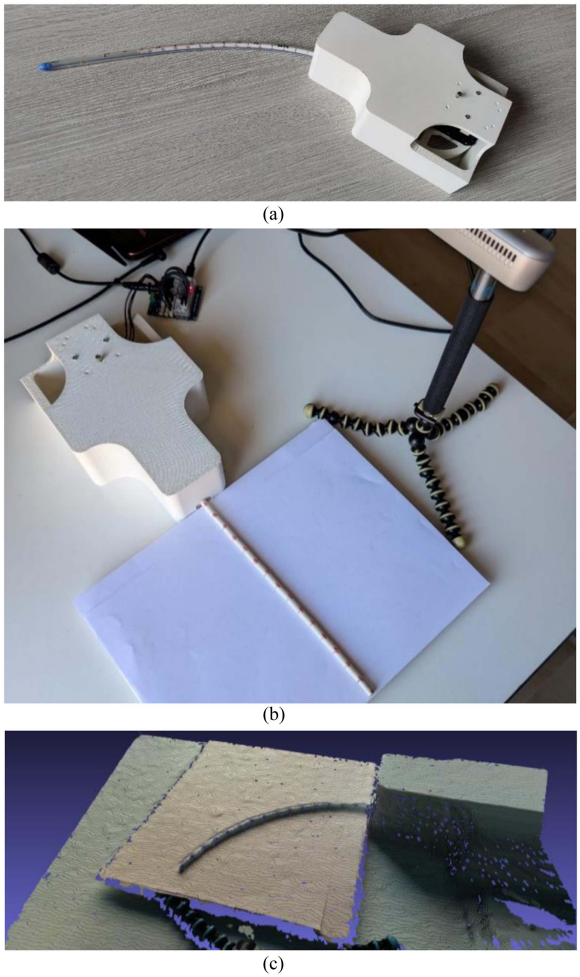

Fig. 9. Robot prototype: (a) Inside a chest tube; (b) experimental layout to evaluate model accuracy; (c) example of an RGB-D point cloud acquired with the 3D camera.

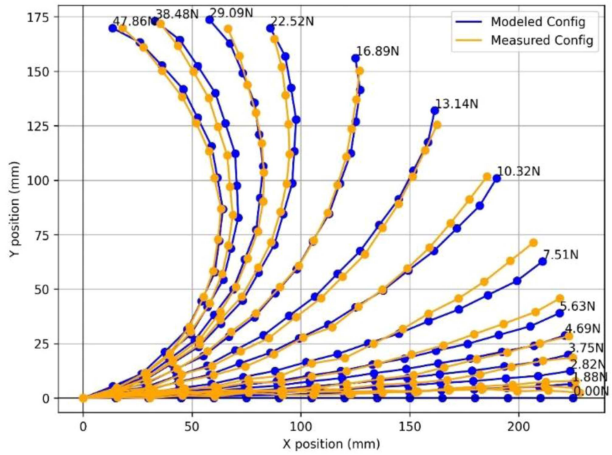

Fig. 10. Comparison between modeled and measured configurations during the planar motion, with 2.25% modeling error on the optimized model.

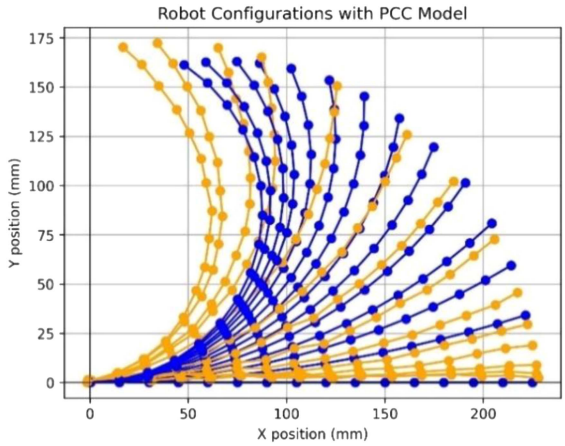

Fig. 11. PCC modeling results during the planar motion.

IV. Results and Discussion

A. Experimental Results

To evaluate the accuracy of the proposed modeling approach and the asymmetric design's capability to bend the tube, a prototype of the first section was fabricated and tested inside the tube to ensure that it meets requirements with a reasonable actuation force (Fig. 9(a)). Then, a setup (Fig. 9(b)) was prepared to measure the robot's configurations and actuation forces within its range of motion. The Dynamixel MX-64T motor's embedded torque sensor measures actuation force. An Intel Realsense 3D camera measures the coordinates of key markers on the robot. A Python program was coded to convert 3D camera data to a point cloud (Fig. 9(c)), where the coordinates can be measured and processed.

The modeling error was defined as the Euclidean distance of each modeled point with its measured value divided by its distance from the base link. Subsequently, model parameters, such as friction coefficient, were calibrated with an optimization that minimized the modeling error. Then, the model was compared with the experiments in Fig. 10, showing a 2.25% error during the planar motion. For comparison, the robot was modeled in the same scenario with piecewise constant curvature (PCC) kinematics, the most common method for modeling continuum robots [16]. Also, in this case, the model parameters were optimized, and the results are demonstrated in Fig. 11, showing a modeling error of 11.45%, over five times that of the proposed modeling approach.

The robot was also tested in a hanging configuration to evaluate the effects of gravity, resulting in an increase in modeling error to about 3.60% (Fig. 12). During this test, the twisting motion and tendon clearance had a more significant influence, giving rise to increased measurement errors mostly attributable to low manufacturing precision and varying assembly conditions. The actuation forces are decreased due to the reduced friction.

B. Discussion

The system proved effective in actuating the catheter, with the proposed design with asymmetric joints providing the expected range of motion without experiencing significant buckling. This asymmetric profile thus results in a simple and effective alternative to other asymmetric features that have already been used in

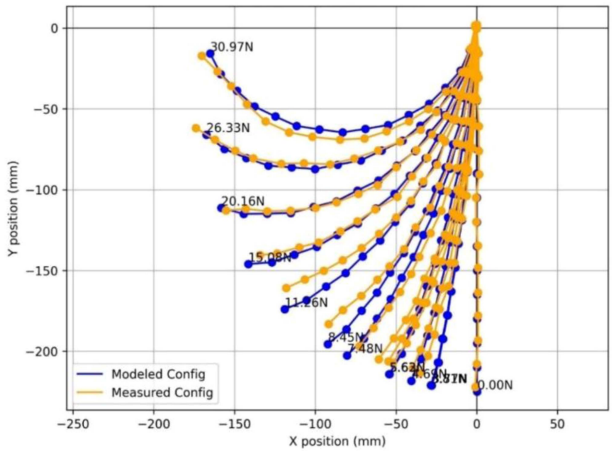

Fig. 12. Modeling results when the robot is hanging.

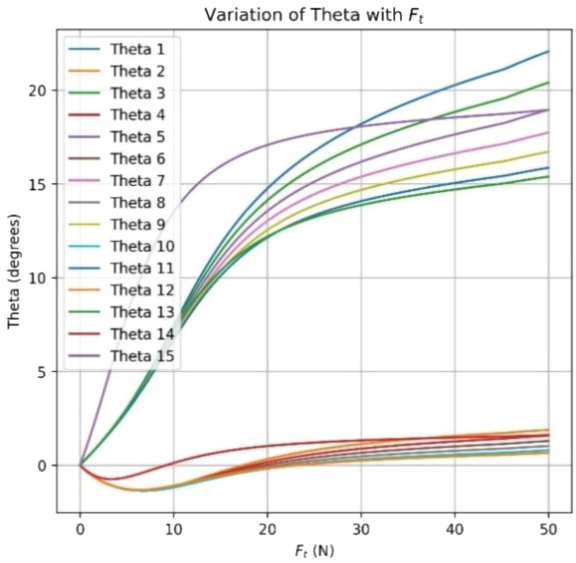

Fig. 13. Variation of the bending angle of the joints with the tension force.

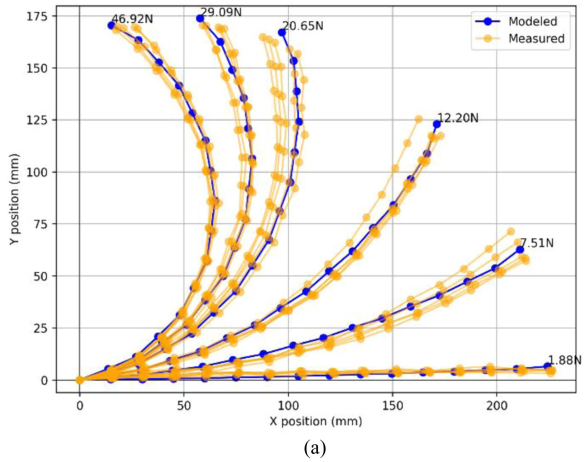

(a)

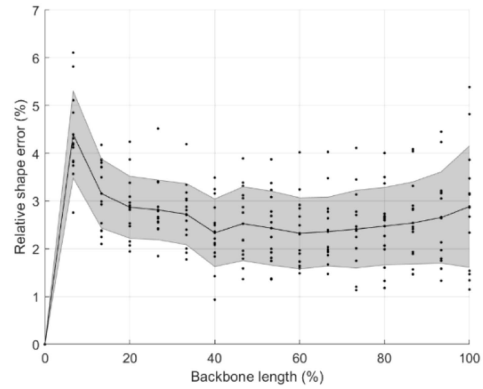

(b)

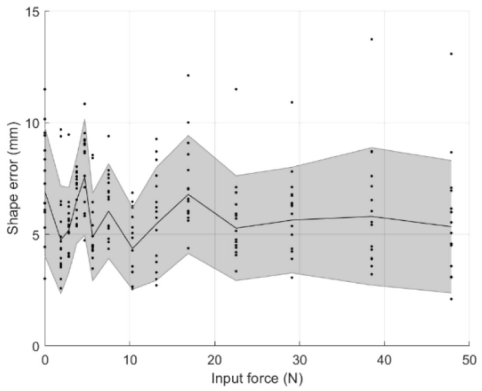

(c)

Fig. 14. Repeatability: (a) Repeated poses; (b) relative shape error at different backbone lengths (mean in back, standard deviation in grey); (c) absolute shape error at different actuation forces (mean in back, standard deviation in grey).

continuum robotics (e.g., backbone asymmetry [17] or routing asymmetry [18]). These previous solutions exploit asymmetry to obtain complex backbone shapes with a limited number of motors; conversely, the proposed asymmetry maintains a circular backbone shape under load while increasing mechanical advantage.

In addition to its kinetostatic behavior, the system also fulfills the medical requirements: the entire system can be detached from the actuation unit by releasing four clamping screws and disposed of. The expendable part is made of 3D printed material (which can also be easily adapted to molding or alternative manufacturing technologies) and inexpensive NiTi rods, for a total cost estimated at less than $10.00 per prototype at the time of writing.

The proposed model performs significantly better than PCC, while still maintaining a much lower computational cost than exact geometrical models (e.g., Cosserat [11], [18]). An average time of 23.16 ms per configuration is observed with the proposed model, computed on a laptop with an Intel 6700hq core i7 with 16GB RAM; the average was computed over a sequence of 14 configurations repeated 1000 times. In comparison, the PCC model requires approximately 1.15 ms per repetition. This difference is due to the PCC model only computing a single bending variable per position, ignoring differences between the segments and the statics of the structure (resulting in higher errors for higher loads; see the bent positions in Fig. 11). Further, the initial iteration of the proposed method is observed as significantly slower than the others, as successive configurations use the previous ones as initial solutions, significantly speeding the algorithm up.

The advantage of the proposed model in capturing the behavior of the system segment by segment is better illustrated in Fig. 13, which depicts the results of how the joint bending angles vary by increasing the tension force.

The different behavior of the three joint categories is clear. The bottom of the diagram shows the behavior of the joints associated with buckling, which oppose the robot's motion at first but return to the normal motion when the tension force exceeds 20 N. Buckling peaks around 6.8 N of tension force for most of the even-numbered joints and its maximum value is maintained at about −1.4 degrees, demonstrating the efficacy of using Nitinol rods to mitigate buckling. Odd-numbered joints bend faster at lower forces, but the bending slows down at larger forces due to friction build-up and increased elastic force.

Further information on system repeatability can be extracted by analyzing acquisition results over multiple repetitions (Fig. 14), where five separate tests have been performed.

Each test consists of data for 16 points equally spaced along the backbone at 14 different instants in time, each corresponding to a different actuation force. The overall performance can be evaluated through tip position error, computed as the displacement between the acquired and modeled tip position, and as shape error, computed as the average displacement of the acquired positions for the 16 control points from the modeled ones. Overall, the average tip positioning error is 2.88%, with a standard deviation of 1.22% (relative to backbone length); the shape error is 2.55%, with a standard deviation of 0.72%. Further information can be extracted by observing the position error at different backbone lengths (Fig. 14(b)): the most proximal segment of the robot shows the worst behavior; the mean error then quickly decreases and increases again, together with the standard deviation, towards the robot tip. Finally, Fig. 14(c) shows how performance is consistent in different configurations and at different actuation forces. Overall, these values highlight robust, repeatable behavior, as shown in the six sample positions reported in Fig. 14(a).

V. Conclusion

This article presents a continuum robot design to guide chest tubes during thoracostomy to reduce its complication rates. The proposed design enhances existing chest tubes with active shape control thanks to an actuated core made of a lean continuum robot

In future work, minimizing the twist motion observed in the system during the preliminary experiments could notably improve the robot's accuracy and repeatability to facilitate better control. From a modeling perspective, introducing non-linear material behavior (i.e., Nitinol superelasticity) will also contribute to higher accuracy. Once refined the design, the system will be tested on anatomical phantoms to develop a user-friendly control interface with a realistic demonstration.

Acknowledgment

We would like to thank Dr. Sebastiano Angelo Bastoni and Dr. Cristiano Casciani of the Thoracic Surgery Unit of the Tor Vergata University Hospital, led by Prof. Vincenzo Ambrogi, who supported this study with their medical expertise.

References

[1] D. Anderson, S. A. Chen, L. A. Godoy, L. M. Brown, and D. T. Cooke, "Comprehensive review of chest tube management: A review," *JAMA Surg.*, vol. 157, no. 3, pp. 269–274, Mar. 2022, doi: 10.1001/jamasurg.2021.7050.

[2] P. E. Dupont, N. Simaan, H. Choset, and C. Rucker, "Continuum robots for medical interventions," *Proc. IEEE*, vol. 110, no. 7, pp. 847–870, Jul. 2022, doi: 10.1109/JPROC.2022.3141338.

[3] J. Burgner-Kahrs, D. C. Rucker, and H. Choset, "Continuum robots for medical applications: A survey," *IEEE Trans. Robot.*, vol. 31, no. 6, pp. 1261–1280, Dec. 2015, doi: 10.1109/TRO.2015.2489500.

[4] "Chest tube insertion," 2024. Accessed: Mar. 27, 2024. [Online]. Available: https://medlineplus.gov/ency/presentations/100008_3.htm

[5] M. T. Mubarak, I. Ozsahin, and D. U. Ozsahin, "Evaluation of sterilization methods for medical devices," in *Proc. Adv. Sci. Eng. Technol. Int. Conferences*, Mar. 2019, pp. 1–4, doi: 10.1109/ICASET.2019.8714223.

[6] R. E. Harrington, T. Guda, B. Lambert, and J. Martin, "3.1.4 - Sterilization and disinfection of biomaterials for medical devices," in *Biomaterials Science*, 4th ed., W. R. Wagner, S. E. Sakiyama-Elbert, G. Zhang, and M. J. Yaszemski, Eds. San Diego, CA, USA: Academic, 2020, pp. 1431–1446, doi: 10.1016/B978-0-12-816137-1.00091-X.

[7] M. H. Baumann, "What size chest tube? What drainage system is ideal? and other chest tube management questions," *Curr. Opin. Pulmonary Med.*, vol. 9, no. 4, pp. 276-281, Jul. 2003.

[8] H. T. Harcke, L. A. Pearse, A. D. Levy, J. M. Getz, and S. R. Robinson, "Chest wall thickness in military personnel: Implications for needle thoracentesis in tension pneumothorax," *Mil. Med.*, vol. 172, no. 12, pp. 1260–1263, Dec. 2007, doi: 10.7205/MILMED.172.12.1260.

[9] E. Schroeder et al., "Average chest wall thickness at two anatomic locations in trauma patients," *Injury*, vol. 44, no. 9, pp. 1183–1185, Sep. 2013, doi: 10.1016/j.injury.2013.03.027.

[10] I. D. Walker, "Robot strings: Long, thin continuum robots," in *Proc. IEEE Aerosp. Conf.*, Mar. 2013, pp. 1–12, doi: 10.1109/AERO.2013.6496902.

[11] M. Russo et al., "Continuum robots: An overview," *Adv. Intell. Syst.*, vol. 5, no. 5, 2023, Art. no. 2200367, doi: 10.1002/aisy.202200367.

[12] T. da Veiga et al., "Challenges of continuum robots in clinical context: A review," *Prog. Biomed. Eng.*, vol. 2, no. 3, Jul. 2020, Art. no. 032003, doi: 10.1088/2516-1091/ab9f41.

[13] M. Wang, X. Dong, W. Ba, A. Mohammad, D. Axinte, and A. Norton, "Design, modelling and validation of a novel extra slender continuum robot for in-situ inspection and repair in aeroengine," *Robot. Comput.-Integr. Manuf.*, vol. 67, Feb. 2021, Art. no. 102054, doi: 10.1016/j.rcim.2020.102054.

[14] D. A. Troncoso et al., "A continuum robot for remote applications: From industrial to medical surgery with slender continuum robots," *IEEE Robot. Automat. Mag.*, vol. 30, no. 3, pp. 94–105, Sep. 2023, doi: 10.1109/MRA.2022.3223220.

[15] J. Legrand, M. Ourak, T. Vandebroek, and E. Vander Poorten, "A large displacement model for superelastic material side-notched tube instruments," *Int. J. Mech. Sci.*, vol. 197, May 2021, Art. no. 106329, doi: 10.1016/j.ijmecsci.2021.106329.

[16] R. J. Webster and B. A. Jones, "Design and kinematic modeling of constant curvature continuum robots: A review," *Int. J. Robot. Res.*, vol. 29, no. 13, pp. 1661–1683, Nov. 2010, doi: 10.1177/0278364910368147.

[17] J. Barrientos-Diez, M. Russo, X. Dong, D. Axinte, and J. Kell, "Asymmetric continuum robots," *IEEE Robot. Automat. Lett.*, vol. 8, no. 3, pp. 1279–1286, Mar. 2023, doi: 10.1109/LRA.2023.3238890.

[18] D. C. Rucker and R. J. Webster III, "Statics and dynamics of continuum robots with general tendon routing and external loading," *IEEE Trans. Robot.*, vol. 27, no. 6, pp. 1033–1044, Dec. 2011.